



An improved shadow measurement technique for constraining the morphometry of simple impact craters

JOHN E. CHAPPELOW* AND VIRGIL L. SHARPTON

Geophysical Institute, University of Alaska Fairbanks, 903 Koyukuk Drive, P.O. Box 757320 Fairbanks, Alaska 99775-7320, USA

*Correspondence author's e-mail address: john.chappelow@gi.alaska.edu

(Received 2001 July 13; accepted in revised form 2001 December 10)

Abstract—The lengths of the shadows cast within simple, bowl-shaped impact craters have been used to constrain their depths on a variety of planetary bodies. This technique, however, only yields the "true" crater depth if the shadow transects the crater center where the floor is deepest. In the past, attempts have been made to circumvent this limitation by choosing only craters where the shadow tip lies very near the crater center; but this approach may introduce serious artifacts that adversely affect the slope of the regressed depth vs. diameter data and its variance. Here we introduce an improved method for deriving depth information from shadow measurements that considers three basic shape variations of simple craters: paraboloidal, conical, and flat-floored. We show that the shape of the cast shadow can be used to constrain crater shape and we derive improved equations for finding the depths of these simple craters.

INTRODUCTION

Impact crater morphometry is a powerful tool, which is often relied upon for deriving information about planetary surface evolution (*e.g.*, Cintala, 1977; Hale and Head, 1979, 1980; Sharpton, 1997) and gaining insights into the impact process itself (*e.g.*, Pike, 1980a,b; Oberbeck, 1971; Herrick *et al.*, 1997). Generally, craters are classified according to their shape, which, because of the influence of gravity, is dependent upon crater size (*e.g.*, Melosh, 1980, 1989). At small diameters, morphologically "fresh" craters are usually simple bowl-shaped depressions with raised rims. The shapes of larger complex craters are affected by late-stage collapse of the original deep craterform, thus producing a final shape characterized typically by terraced walls, a shallow floor, and central structures, such as peaks and one or more concentric rings (*e.g.*, Pike, 1980b; Melosh, 1989). The transitional diameter between simple and complex craters is inversely related to the target body's surface gravity (*e.g.*, Pike and Arthur, 1979; Pike, 1980a); for Earth the transition to the complex craterform occurs at diameters between 2 and 4 km (*e.g.*, Dence *et al.*, 1977); for the Moon, it is between 15 and 20 km (*e.g.*, Pike, 1971, 1974).

The shape of simple craters is thought to superficially resemble the shape of the original "transient" crater (*e.g.*, Melosh, 1989) (*i.e.*, the initial cavity formed by the effects of excavation and structural displacements of the impacted target). Furthermore, studies have shown that the shapes of simple craters can vary with impact velocity (*e.g.*, Oberbeck, 1971, 1977) and target characteristics (*e.g.*, Quaide and Oberbeck, 1968; Oberbeck, 1977; Mouginiis-Mark and Hayashi, 1991),

such as strength, presence of layering, *etc.* Consequently, understanding the morphometry of such features is of particular interest. A classic means of characterizing craters is to measure the rim-to-floor depth as a function of crater diameter. Stereogrammetry (*e.g.*, Pike, 1974; Herrick and Sharpton, 2000) and photoclinometry (*e.g.*, Davis and Soderblom, 1984; Schenk, 1989; Craddock *et al.*, 1997) have both been used to determine crater depths and morphologies, but both methods have limitations. Stereogrammetry requires at least two images of the target area, taken from different angles, making it difficult to apply in general to most of the solid bodies in the solar system. Photoclinometry requires knowledge of the target's photometric function; changes in albedo across a feature can severely affect the accuracy of the resulting measurement. Both of these methods are adversely affected by atmospheric scattering, and by the presence of shadows in images taken at low-Sun angles.

Cast shadows provide an independent means of measuring crater depths and shadow measurements have been widely used to determine crater depths on many solar system bodies (*e.g.*, Arthur, 1974; Pike, 1980a; Pike and Clow, 1983; Schenk, 1989). This method is complementary to the other methods of constraining crater depths in that it requires only one image and works for images taken at lower Sun angles. It is also simple: consider a simple crater exhibiting a shadow that is exactly half the crater diameter (D) in length as shown in Fig. 1. The crater rim-to-floor depth (d) can be determined from the following simple equation:

$$d = L / \tan \theta \quad (1)$$

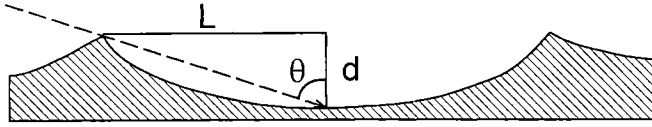


FIG. 1. An idealized cross section showing a shadow of width $D/2$ cast inside a simple crater.

or to get the depth-to-diameter ratio:

$$\frac{d}{D} = \frac{L}{D \tan \theta} \quad (2)$$

where L is the shadow length, measured from the crater rim to the floor and θ is the solar incidence angle measured from the vertical.

Inspection of Fig. 1 shows that this method only measures the true crater depth if the shadow edge passes through the crater center. For this reason crater depth studies usually include only craters in which the shadow edge lies very near the crater center (e.g., Arthur, 1974; Pike, 1980a; Pike and Clow, 1983), typically within $0.05D-0.10D$ of the center, to limit the error due to crater shape. However, this crater selection process itself may produce serious artifacts. Choosing a sample of craters based on whether or not they show shadows lengths approximately equal to $D/2$ is equivalent to artificially constraining the depth-to-diameter ratio, d/D , for any given solar incidence angle. Consider, for example, a case where only simple craters for which $L = D/2 \pm 0.05D$ are measured. The limits on d/D are determined from Eq. (2):

$$\left(\frac{d}{D}\right)_{\max} = \frac{0.5D + 0.05D}{D \tan \theta} = \frac{0.55}{\tan \theta};$$

$$\left(\frac{d}{D}\right)_{\min} = \frac{0.5D - 0.05D}{D \tan \theta} = \frac{0.45}{\tan \theta}$$

For a given value of θ , these limits are fixed. Hence, by selecting only those craters whose shadows fall near their centers, all craters that are shallower or deeper than this narrow range of d/D are excluded from the analysis.

A graph of d vs. D for the measured craters will be a straight line population, with an artificial slope of $(2 \tan \theta)^{-1}$ because the selection process has excluded craters that do not lie near this line. The conventional $\log(d)$ vs. $\log(D)$ graph will be a straight line with a slope approaching unity—irrespective of what the actual depth vs. diameter trend may be. The scatter of the data about this line will also depend on how much the shadow is allowed to deviate from the crater center point. Narrow limits will result in data that cluster near the regression line with artificially low variances and artificially high regression coefficients.

Some attempts have been made to mitigate this effect by either including craters with shadows that are considerably longer or shorter than $D/2$, or adding an empirical correction

factor to the value of d arrived at using Eq. (1) (e.g., Pike, 1980a). Both methods potentially impart errors that are poorly constrained.

For large enough study areas, or if several images of a smaller study area are available, θ could vary, allowing measurements of craters of various d/D ratios to be made. However in the first case one must assume that the d/D distribution is constant over a large study area, and within any region of approximately constant θ , the only craters measured will still be those with appropriate d/D values. Thus each d/D value will represent a region of the image. No account is taken for any anomalously deep or shallow craters in a given region, and regional variations in the d/D distribution will not be seen. In addition, foreshortening of craters may cause severe problems in making measurements, if the images are not orthorectified. In the second case, several images of the study area, taken at different incidence angles are required, but are often not available.

Here, we derive a more precise and general method of constraining simple crater depths that does not require the shadow edge to be near the crater center nor is it limited to any particular size or number of images. The problem of foreshortening may be avoided by using nadir-looking or orthorectified images. By assuming reasonable, mathematically simple shapes (paraboloid, cone, flat-floored) for simple craters we can derive equations that describe the shapes of the shadows cast inside them. The shapes of actual shadows can then be used to classify the shapes of simple craters and to constrain the craters' depths.

SHADOWS IN PARABOLIC CRATERS

Laboratory impact experiments (Oberbeck, 1971, 1977) and morphometric studies of actual impact craters relying upon photogrammetry indicate that simple craters normally are closely approximated by a paraboloid (Oberbeck, 1971) with shape defined by the equation:

$$z(r) = A(x^2 + y^2) = Ar^2 \quad (3)$$

where the origin is the center of the crater floor. Herein, the positive z -axis is up, the x -axis is perpendicular to z and points in the direction opposite the solar azimuth, and y forms a right-handed orthogonal coordinate system with x and z . The constant A is arbitrary and r is the perpendicular distance from the z -axis. Evaluating Eq. (3) at the point $x = R$, $y = 0$, $z = d$ yields $A = d/R^2$. Consequently:

$$z(r) = \frac{d}{R^2}(x^2 + y^2) = \frac{d}{R^2}r^2 \quad (4)$$

where R is the radius of the crater and d its depth.

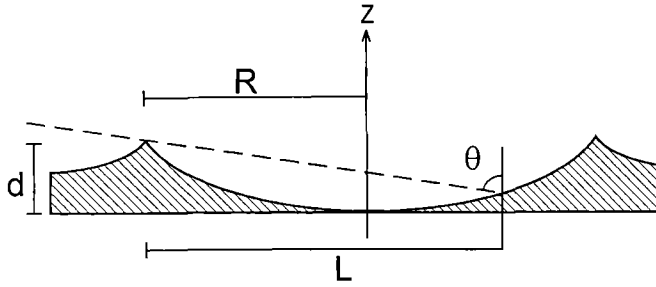


FIG. 2. Section through a paraboloidal crater. The bold arrow signifies a solar ray which passes just over the sunward rim of the crater and defines the shadowed area.

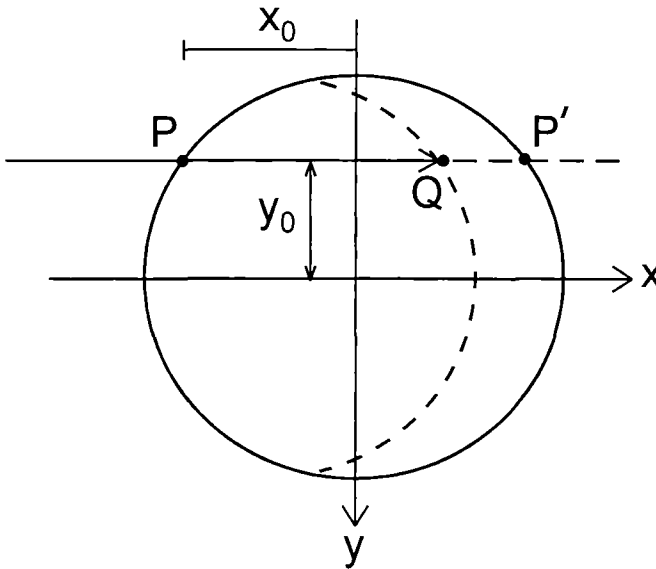


FIG. 3. A plan view of a solar ray passing just over the rim of the crater at P and incident on point Q inside the crater. Note that the section P-P' is not constrained to pass through the center of the crater as all sections of a paraboloid that are parallel to its symmetry axis are parabolas. The dashed line signifies the shadow boundary.

As shown in Figs. 2 and 3, the shaded area of such a simple crater is defined by a solar ray, which passes just over the crater rim at point P (coordinates (x_0, y_0, z_0)) and intersects the crater floor at point Q (coordinates (x, y, z)). The locations of all such points Q define the shadow boundary. This boundary can be mathematically described by equations of the form $z = z(x, y(x))$, the solution of which will be in the form of Eq. (4), and $y = y(x)$, which describes the plan view of the shadow. Employing the tangent function and assuming (1) that the crater rim is perfectly circular and horizontal, with height $z = d$ and (2) that solar rays are parallel (*i.e.*, the crater is far from the Sun):

$$x_0 = -\sqrt{R^2 - y_0^2} \tag{5a}$$

and

$$y_0 = y \tag{5b}$$

Consequently, from the definition of $\tan\theta$:

$$z = d - \frac{x + \sqrt{R^2 - y^2}}{\tan\theta} \tag{6}$$

Then, combining Eqs. (4) and (6) eliminates z from the equation. The result may be written:

$$\frac{d \tan\theta}{R^2} x^2 + x - d \tan\theta + \frac{d \tan\theta}{R^2} y^2 = -\sqrt{R^2 - y^2} \tag{7}$$

Eq. (7), which relates the x and y coordinates of any point on the shadow boundary, has two solutions:

$$y_1(x) = \pm\sqrt{R^2 - x^2} \tag{8a}$$

and

$$y_2(x) = \pm\sqrt{R^2 - (x + R^2/d \tan\theta)^2} = \pm\sqrt{R^2 - (x - x_C)^2} \tag{8b}$$

where

$$x_C = -\left(\frac{R}{d \tan\theta}\right)R = -\left(\frac{D}{4d \tan\theta}\right)D \tag{9}$$

Eq. (8a,b) fully describe the boundary of the shadow, as viewed from above. Both are circles of radius R in the x - y plane. The first is centered at the origin, coincides with the crater rim and forms the boundary of the shadow in the sunward direction. The other, the shadow boundary circle, forms the rest of the shadow boundary and is centered at $x = x_C, y = 0$. The intersection of these circles is the shadowed area (Fig. 4).

We can now describe what the shadow looks like and how it evolves as the Sun rises over the crater. At sunrise over the crater θ is 90° , $\tan\theta$ is infinite, and x_C is zero (*i.e.*, the circles described by Eqs. (8a,b) coincide and shadow fills the crater). As the Sun rises, θ and $\tan\theta$ decrease, x_C increases in the negative direction, and the shadow boundary circle shifts in the direction of the Sun. The shadow, bounded by the arcs of the two circles, diminishes (Fig. 5a). When $\tan\theta$ falls to R/d in magnitude, x_C becomes $-R$, and the shadow intersects the center of the crater (Fig. 5b). This is the special case where the depth calculated from Eq. (1) is correct.

Finally, when $\tan\theta = R/2d$, $x_C = -2R$, the circles become tangent to each other and the shadow disappears completely

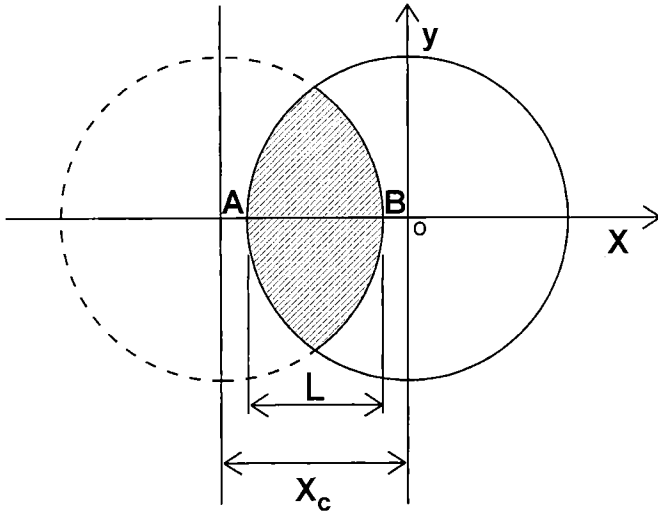


FIG. 4. An overhead view of the two circles that define the shadow; the solid circle is also the crater rim. The other, the shadow boundary circle, is displaced a distance x_c to the left relative to the crater rim.

(Fig. 5d). At this point the solar elevation angle is greater than the slope of the top of the crater rim and the entire interior of the crater is illuminated. This value of θ marks the absolute lower limit of the usefulness of any shadow method of depth determination for parabolic craters because for $\theta < \tan^{-1}(R/2d)$ there is no shadow in the crater.

Shadow length L is simply the distance between point A, at $x = -R$, and point B at $x = x_c + R$ (Fig. 4). Consequently,

$$L = 2R - \frac{R^2}{d \tan \theta}$$

and

$$d = \frac{D}{4(1 - L/D) \tan \theta} \tag{10}$$

for a parabolic crater.

SHADOWS IN CONICAL CRATERS

Cone-shaped craters are another common variety of simple crater, possibly caused by relatively low velocity impacts (Oberbeck, 1971). The shape of a conical crater is given by:

$$z = \left(\frac{d}{R}\right) \sqrt{x^2 + y^2} \tag{11}$$

Inserting this crater shape into Eq. (6) yields:

$$\left(\frac{d}{R}\right) \tan \theta \sqrt{x^2 + y^2} = d \tan \theta - x + \sqrt{R^2 - y^2} \tag{12}$$

The solutions of this equation are the circle:

$$x^2 + y^2 = R^2$$

which represents the rim, and the ellipse:

$$\frac{(x - x_c)^2}{\alpha^2 R^2} + \frac{y^2}{R^2} = 1 \tag{13}$$

where:

$$\alpha = \left[\frac{\left(\frac{d \tan \theta}{R}\right)^2 + 1}{\left(\frac{d \tan \theta}{R}\right)^2 - 1} \right] \tag{13a}$$

and

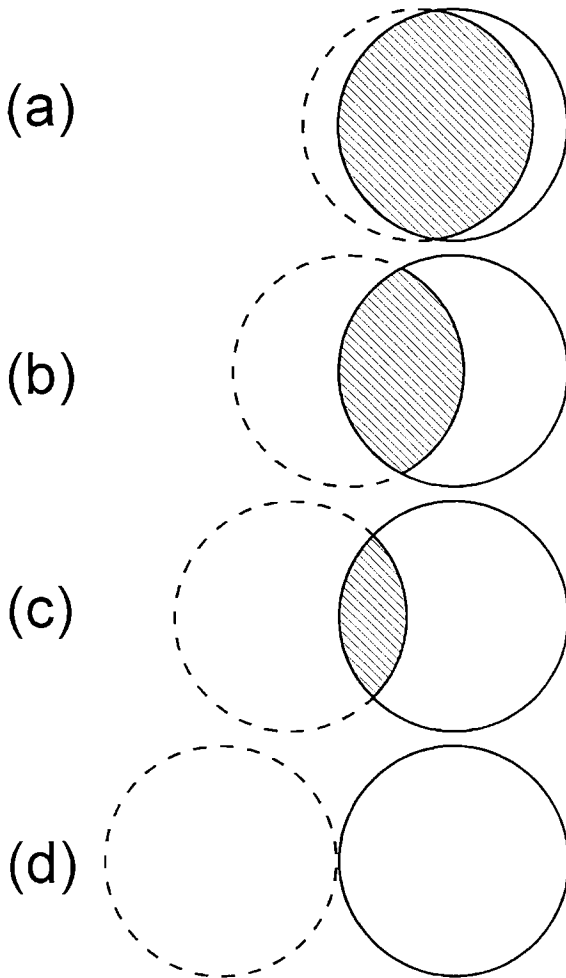


FIG. 5. The evolution of the shadow as the Sun rises over a simple, parabolic crater.

$$x_C = -\frac{2\left(\frac{d \tan \theta}{R}\right)}{\left(\frac{d \tan \theta}{R}\right)^2 - 1} R \quad (13b)$$

which forms the other shadow boundary (Fig. 6).

As in the circular case, we can now describe the evolution of this shadow with increasing Sun angles. As the Sun rises above the crater rim, the ellipse extends along the surface in the illumination direction, becoming increasingly eccentric, as shown in Fig. 7. Finally, when $\theta = \tan^{-1}(R/d)$, the solar incidence angle is greater than the slope of the crater walls and the entire crater is illuminated.

Using the same method as in the previous section, we derive an equation for the depth of a conical crater:

$$d = \frac{L}{2(1-L/D)\tan \theta} \quad (14)$$

SHADOWS IN CRATERS WITH FLAT BOTTOMS

The effect of a flat bottom on the shadow inside a crater can be seen by considering the parallel rays from a light source (Sun) incident on two parallel planes at some incidence angle θ (Fig. 8). The upper plane contains a hole of diameter D and corresponds to the crater rim, while the lower plane represents the flat bottom of the crater. An illuminated circle of diameter D will be projected onto the lower plane, displaced away from the Sun by an amount x_C :

$$x_C = d' \tan \theta$$

where d' is the separation of the two planes. A flat region at the bottom of a crater will be illuminated in the same way (Fig. 9).

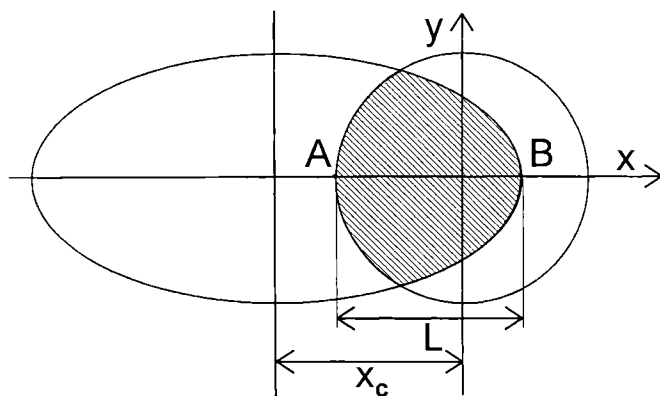


FIG. 6. The shadow geometry in a cone shaped crater.

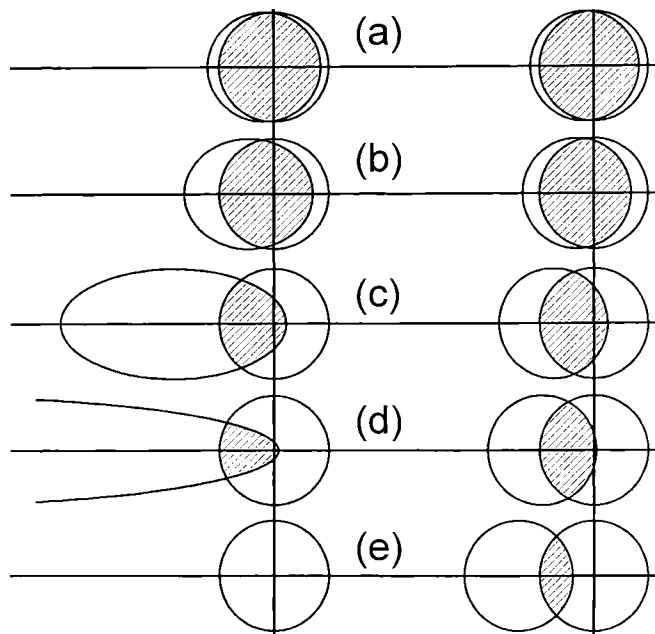


FIG. 7. A comparison of the shadows in parabolic (right) and conical (left) craters with $d/D = 0.20$. The incidence angles are (a) 89° (b) 83° (c) 77° (d) 71° (e) 60° .

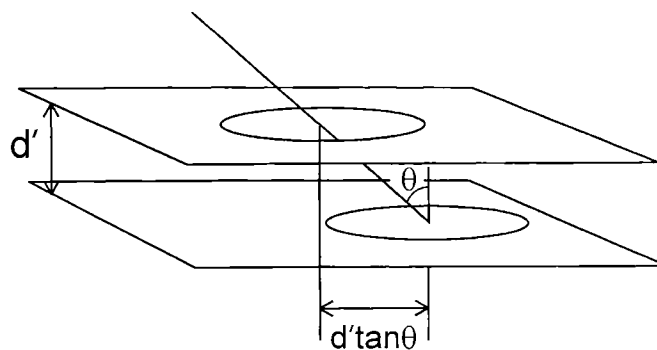


FIG. 8. The projection of a circle (crater rim) onto a plane (flat crater bottom).

APPLICATIONS

In this section, we illustrate the utility of the shadow analysis technique derived above by examining three lunar craters, as represented in Clementine imagery. We will use shadow shape to determine the simple shape that most closely fits the crater and then constrain its depth. In all three of the craters (Fig. 10a-c), the crater axes, crater rims and shadow boundary shapes are marked. All images have been rotated so that solar illumination is from the $-y$ direction.

The crater in Fig. 10a has $D = 19\,900$ m, $L = 15\,200$ m and is illuminated at $\theta = 82.6^\circ$. The circular shadow boundary indicates that the crater is parabolic in shape (compare to Fig. 4),

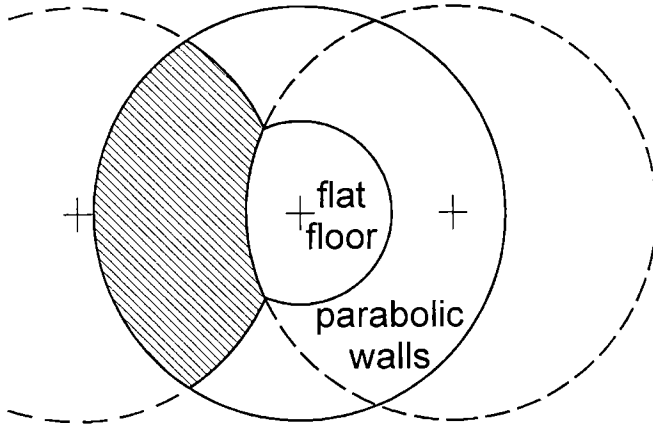


FIG. 9. The effect of a flat bottom on the shape of the shadow inside a parabolic crater. Crosses mark the centers of (left to right) the shadow boundary circle, the crater center, and the flat bottom illumination boundary circle. The effect on the elliptical shadow boundary in a conical crater is identical.

so from Eq. (10), $d = 2700$ m and d/D is 0.13. Note that d is a maximum depth constraint, because constraints on the parabolic shape only apply to the sunlit portion of the crater interior. Unless additional, higher Sun angle imagery is available to determine the configuration of the shadowed region of the crater bottom, the possibility that the crater floor could flatten out immediately inside the shadowed region cannot be dismissed. In this case, the maximum diameter of a hidden flat bottom would be $D_f = 2L - D = 10\,500$ m and the minimum depth of the crater is given by:

$$d_{\min} = \left(1 - \frac{D_f^2}{D^2}\right)d$$

or, more simply, by $d_{\min} = L/\tan \theta = 2000$ m, from Eq. (1). The minimum value of d/D is 0.10.

The shadow in crater Fig. 10b is fit well by an ellipse, not by a circle, showing that it is conical in shape (compare to Fig. 7). Its diameter is 15 500 m, $L = 9700$ m and $\theta = 72.0^\circ$. From Eq. (14) the maximum depth, d , is 4200 m giving a maximum $d/D = 0.27$. If a flat floor with the maximum permissible diameter of $D_f = 3900$ m is assumed, the minimum permissible depth is simply:

$$d_{\min} = \left(1 - \frac{D_f}{D}\right)d$$

Using this equation, or Eq. (1), the minimum depth is 3100 m, giving a minimum $d/D = 0.20$. These examples illustrate a limitation of the shadow measurement technique: the farther the shadow extends beyond the crater center the greater the potential for error due to unseen topography. In both cases the term D_f/D is a measure of the potential error.

Figure 10c shows a crater with a conspicuous flat bottom. The effect of the flat bottom on the shadow shape is clearly visible (compare to Fig. 9). The sides of the shadow are best fit with an ellipse, indicating that the crater walls are probably conical, although the limited length of the contact between the shadow and the fit leaves this interpretation open to question. The diameter is 14 100 m and the shadow length along the y -axis is 6100 m. From Eq. (1) the depth is 1600 m, giving $d/D = 0.11$. Note in all three of these cases that the shape of the shadow is used only to select the proper crater shape, if any, for the depth calculation. There is no need to actually fit a curve to the shadow edge.

In Fig. 10, a darkening of the ends of the illuminated crescents inside the crater is apparent. These dark broad "wings" indicate that rims of real craters are usually rounded and, therefore, deviate from the simple shapes assumed here. The points along the shadow edge, where it begins to broaden, indicate the locations where the wall-rim slopes begin to shallow and rounding begins. This could be a useful morphometric indicatrix: for instance the size of the shadow "wings" could be used to determine how rounded (and, therefore, how modified) the crater rim is.

CONCLUSIONS

(1) Previously used shadow methods of measuring crater depths suffer from the fact that the currently used formula for the depth is only useful when the shadow boundary passes near to the center of the crater. This method may introduce artifacts, because, for any fixed solar incidence angle, the selection process is equivalent to selecting only craters that fall within a very narrow range of d/D , where d is the depth and D the diameter.

(2) Parabolic craters show shadow shapes that are defined by the intersection of two circles, both with diameters equal to the crater rim diameter. The equation for determining the maximum depth of a parabolic crater is:

$$d = \frac{D}{4(1 - L/D)\tan \theta}$$

where L is the shadow length and θ the solar incidence angle.

(3) Craters with conical walls show shadows that are defined by the intersection of the crater rim and an ellipse whose semi-minor axis is the same as the crater rim diameter and whose semi-major axis is dependent on the solar incidence angle. The maximum of depth a conical crater is given by:

$$d = \frac{L}{2(1 - L/D)\tan \theta}$$

(4) The equations for the depths of both of these craters actually represent upper bounds on the depth, since any

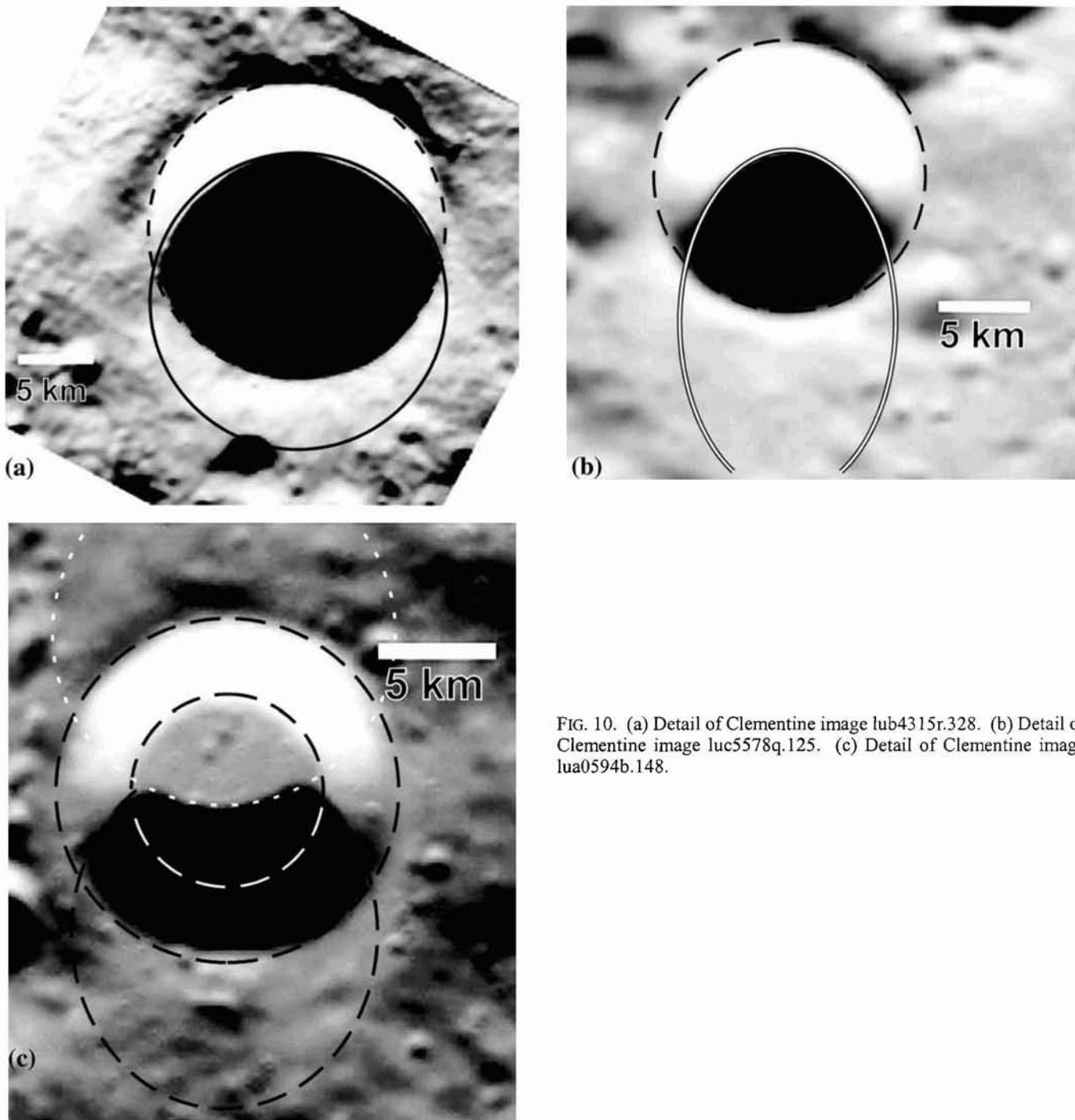


FIG. 10. (a) Detail of Clementine image lub4315r.328. (b) Detail of Clementine image luc5578q.125. (c) Detail of Clementine image lua0594b.148.

topography not crossed by the shadow boundary, particularly flat bottoms, cannot be accounted for using this method. When the shadow edge crosses a flat bottom, the simple equation:

$$d = \frac{L}{\tan \theta}$$

gives its depth.

Acknowledgements—This work is part of the Ph.D. thesis research of J. E. C. at the Geophysical Institute of the University of Alaska Fairbanks and was supported by grants to V. L. S. from the NASA Planetary Geology and Geophysics Program (NAG5-9392) and the NASA Mars Data Analysis Program (NAG5-10605). The authors would like to thank P. M. Schenk and an anonymous reviewer for their constructive comments in the review of this work.

Editorial handling: R. A. F. Grieve

REFERENCES

- ARTHUR D. W. G. (1974) Lunar crater depths from Orbiter IV long focus photographs. *Icarus* **23**, 116–122.
- CINTALA M. J. (1977) Martian fresh crater morphology and morphometry—A pre-Viking review. In *Impact and Explosion Cratering* (eds. D. Roddy, R. Pepin and R. Merrill), pp. 575–591. Pergamon Press, New York, New York, USA.
- CRADDOCK R. A., MAXWELL T. A. AND HOWARD A. D. (1997) Crater morphometry and modification in the Sinus Sabaeus and Margaritifer Sinus regions of Mars. *J. Geophys. Res.* **102E**, 13 321–13 340.
- DAVIS P. A. AND SODERBLOM L. A. (1984) Modeling crater topography and albedo from monoscopic Viking orbiter images. *J. Geophys. Res.* **89**, 9449–9457.
- DENCE M. R., GRIEVE R. A. F. AND ROBERTSON P. B. (1977) Terrestrial impact structures: principal characteristics and energy considerations. In *Impact and Explosion Cratering* (eds. D. Roddy, R. Pepin and R. Merrill), pp. 247–275. Pergamon Press, New York, New York, USA.
- HALE W. AND HEAD J. W. (1979) Central peaks in lunar craters: Morphology and morphometry. *Proc. Lunar Planet. Sci. Conf.* **10th**, 2623–2633.
- HALE W. AND HEAD J. W. (1980) Central peaks in mercurian craters: Comparisons to the Moon. *Proc. Lunar Planet. Sci. Conf.* **11th**, 2191–2205.
- HERRICK R. R. AND LYONS S. N. (1998) Inversion of crater morphometric data to gain insight on the cratering process. *Meteorit. Planet. Sci.* **33**, 131–143.
- HERRICK R. R. AND SHARPTON V. L. (2000) Implications from stereo-derived topography of Venusian impact craters. *J. Geophys. Res.* **105E**, 20 245–20 262.
- HERRICK R. R., SHARPTON V. L., MALIN M. C., LYONS S. N. AND FEELY K. (1997) Morphology and morphometry of impact craters. In *Venus II: Geology, Geophysics, Atmosphere and Solar Wind Environment* (eds. S. Bougher, D. Hunten and R. Philips), pp. 1015–1046. Univ. Arizona Press, Tucson, Arizona, USA.
- MELOSH H. J. (1980) Cratering mechanics—Observational, experimental, and theoretical. *Ann. Rev. Earth Planet. Sci.* **8**, 65–93.
- MELOSH H. J. (1989) *Impact Cratering: A Geologic Process*. Oxford University Press, New York, New York, USA. 245 pp.
- OBERBECK V. R. (1971) Laboratory simulation of impact cratering with high explosives. *J. Geophys. Res.* **76**, 5732–5749.
- OBERBECK V. R. (1977) Application of high explosion cratering data to planetary problems. In *Impact and Explosion Cratering* (eds. D. Roddy, R. Pepin and R. Merrill), pp. 45–65. Pergamon Press, New York, New York, USA.
- MOUGINIS-MARK P. J. AND HAYASHI J. N. (1991) Depth/diameter relationships of fresh craters within Hesperia Planum, Mars. *NASA Tech. Memo.* **4300**, 370–372.
- PIKE R. J. (1971) Genetic implications of the shapes of martian and lunar craters. *Icarus* **15**, 384–395.
- PIKE R. J. (1974) Depth/diameter relations of fresh lunar craters: Revision from spacecraft data. *Geophys. Res. Lett.* **1**, 291–294.
- PIKE R. J. (1980a) Control of crater morphology by gravity and target type: Mars, Earth, Moon. *Proc. Lunar Planet. Sci. Conf.* **11th**, 2159–2189.
- PIKE R. J. (1980b) Formation of complex impact craters: Evidence from Mars and other planets. *Icarus* **43**, 1–19.
- PIKE R. J. AND ARTHUR D. W. G. (1979) Simple to complex impact craters: The transition on Mars. *NASA Tech. Memo.* **80339**, 132–134.
- PIKE R. J. AND CLOW G. D. (1983) Ode to gravity: Depth/diameter for fresh craters on Mercury. *NASA Tech. Memo.* **86246**, 104–106.
- QUAIDE W. L. AND OBERBECK V. R. (1968) Thickness determinations of the lunar surface layer from lunar impact craters. *J. Geophys. Res.* **73**, 5247–5270.
- SCHENK P. M. (1989) Crater formation and modification on the icy satellites of Uranus and Saturn: Depth/diameter and central peak occurrence. *J. Geophys. Res.* **94**, 3813–3832.
- SHARPTON V. L. (1997) Evidence from Magellan for unexpectedly deep complex craters on Venus. In *Large Meteorite Impacts and Planetary Evolution* (eds. B. Dressler, R. Grieve and V. Sharpton), pp. 19–27. Geological Society of America, Boulder, Colorado, USA.